

Semantic-ICP: Iterative Closest Point for Non-rigid Multi-Organ Point Cloud Registration

Wanwen Chen, Carson Studders, Jamie J.Y. Kwon, Emily H.T. Pang, Eitan Prisman, and Septimiu E. Salcudean, *Life Fellow, IEEE*

Abstract—Point cloud registration is important in computer-aided interventions (CAI). While learning-based point cloud registration methods have been developed, their clinical application is hampered by issues of generalizability and explainability. Therefore, classical point cloud registration methods, such as Iterative Closest Point (ICP), are still widely applied in CAI. ICP methods fail to consider that: (1) the points have well-defined semantic meaning, in that each point can be related to a specific anatomical label; (2) the deformation required for registration needs to follow biomechanical energy constraints. In this paper, we present a novel semantic ICP (SemiICP) method that handles multiple point labels and uses linear elastic energy regularization. We use semantic labels to improve the robustness of the closest point matching and propose a novel point cloud deformation representation to apply explicit biomechanical energy regularization. Our experiments on a trans-oral robotic surgery ultrasound-computed tomography registration dataset and two public Learn2reg challenge datasets show that our method improves the Hausdorff distance and mean surface distance compared with other point-matching-based registration methods.

Index Terms—Point cloud registration, Iterative Closest Point, Elastic Energy Regularization.

I. INTRODUCTION

REGISTRATION is an important problem in computer-aided intervention (CAI). To enhance visualization of surgical planning, CAI systems require registration of pre-operative volumes to intraoperative volumes, meshes, or surfaces. Point clouds describe critical anatomical structures as spatial points, providing a modality-agnostic, sparse and flexible representation. Point clouds also contain less sensitive information that can identify patients than dense volumes, such as the metadata embedded in DICOM files, addressing privacy concerns in medical practice. Therefore, point cloud registration has been applied in different CAI systems [1].

The work is supported by an NSERC Discovery Grant and the Charles Laszlo Chair in Biomedical Engineering held by Dr. Salcudean, the VCHRI Innovation and Translational Research Awards and the University of British Columbia Department of Surgery Seed Grant held by Dr. Prisman.

Wanwen Chen and Septimiu E. Salcudean are with the Department of Electrical and Computer Engineering, University of British Columbia, Vancouver, BC V6T1Z4 Canada (e-mail: wanwenc@ece.ubc.ca, tims@ece.ubc.ca).

Carson Studders, Jamie J.Y. Kwon, Emily H.T. Pang and Eitan Prisman are with the Faculty of Medicine, University of British Columbia, Vancouver, BC V6T1Z4 Canada (e-mail: studders@student.ubc.ca, jamie.kwon@vch.ca, Emily.Pang@vch.ca, eitan.prisman@ubc.ca).

Deep learning models have emerged in general point cloud registration [2], [3], but they are data-hungry and struggle to generalize to different tasks. A recent study shows that the deep learning model trained on general point clouds cannot be applied to CT patient registration out-of-the-box and has lower performance compared with RANSAC initialization and ICP refinement [4]. Finetuning deep learning models on specific datasets is required to achieve a preferable performance [5]. However, this may not be possible due to the limited training data in a specific CAI application. Another concern regarding deep learning models is that they operate as a black-box, which is suboptimal for medical procedures since explainability can enhance both clinician and patient trust in CAI systems. A generalizable and explainable optimization-based point cloud registration method, therefore, is more preferable in CAI.

One of the most representative optimization-based registration algorithms, Iterative Closest Point (ICP) [6], is widely used in CAI [1] and has been applied in recent navigation systems for spine surgery [7] and oral and maxillofacial surgery [8]. Compared with Gaussian Mixture Models-based registrations [9], point matching-based ICP has a lower computation time, making it preferable in intervention procedures. However, ICP was originally developed for general computer vision that did not utilize medical domain knowledge. First, the semantic information of the point cloud, such as the points' anatomical labels, is not utilized. Second, non-rigid ICP-based registration [10]–[12] regularizes the deformation by local affine regularization, ignoring the underlying biomechanical effects. Addressing these problems, we propose a novel and generalizable point-matching registration method that utilizes the semantic information and introduces explicit linear biomechanical energy regularization.

A. Related Work

1) ICP and its Variants: ICP [6] was developed over 30 years ago, but it is still widely applied in medical point cloud registration for CAI. ICP iteratively finds the closest point pairs in two point clouds, and the corresponding point pairs are used to estimate a rigid transformation to move the source point cloud closer to the target point cloud. The initial alignment between the two point clouds should be close enough to ensure convergence, making ICP sensitive to initialization and outliers, and it tends to get trapped in local minima. To alleviate problems with initialization, Global-

ICP [13] performs a global search over 3D space. Fast-robust-ICP [14] uses Welsch's function to improve the robustness of the error metric. However, these methods estimate rigid transformations, which cannot correct for point cloud deformation, and therefore their utility is limited in medical applications.

To address non-rigid registration, non-rigid ICP [10] extends ICP to estimate the surface deformation using a similar nearest-point search to find the point correspondences. The deformation is regularized using a local affine transformation. It has been used in ultrasound (US)-guided augmented reality navigation for liver procedures [15]. More recent non-rigid ICP registration methods focus on accelerating convergence and increasing robustness. Yao et al. [11] use a deformation graph with a globally smooth robust estimator to regularize the deformation, and then use accelerated optimization to improve the runtime [12]. However, these methods are not regularized by physical parameters; they only consider local affine regularization, which cannot capture the underlying biomechanical characteristics within medical point clouds.

2) Semantic-assisted Point Cloud Registration: Using segmentation for registration is common in 3D volume registration [16]–[18]. Medical images contain rich semantic information, including tissue and organ types, which can be leveraged to improve region matching accuracy. In contrast, using semantic segmentation in point cloud registration remains relatively underexplored, likely due to the difficulty of segmenting traditional point clouds. Zaganidis et al. [19] use PointNet to segment light detection and ranging (LiDAR) point clouds and use the segmentation to aid point matching. Wang et al. [20] segment LiDAR point cloud to cars or the background before performing ICP. However, they use rigid registration, which cannot account for surface deformation. Point clouds derived from medical images can be segmented using various techniques, including deep learning [21], or through novel imaging modalities such as T-modeTM ultrasound, which can identify tissue type automatically [22]. Several studies have explored incorporating segmentation into medical point cloud registration. Hiep et al. [23] segment bones and arteries from US and perform ICP registration on them separately. Thomson et al. [16] segment the hepatic and portal veins, and use Coherent Point Drift to register the vessels independently. These studies do not account for interactions between organs or surrounding tissues, failing to capture their interdependent motion. Jiang et al. [24] use segmentation to align US and computed tomography (CT) of the ribs, and the non-rigid point cloud refinement relies on the specific graph structure of cartilage. A generalizable non-rigid registration method that does not rely on specific structures has a broader application.

3) Biomechanics-inspired Regularization in Point Cloud Registration: Previous work introducing biomechanical constraints into point cloud registration requires sophisticated finite element modeling (FEM). The regularization can be introduced through iterative FEM directly [25]–[27], but FEM is time-consuming and computationally intensive. Data-driven biomechanical models implicitly introduce the constraints by learning from finite element simulation [28]–[30], but the trained models lack generalization to new data. Physics or biomechanics-inspired constraints have been introduced

through a discrete approximation to the continuous elastic energy in 3D voxels [31]–[33]. However, the challenge of introducing this regularization into point cloud registration is that the point clouds only represent the deformation field as surface point movement, which solely describes the boundary conditions of the deformation field. Recently, Heinrich et al. [34], [35] introduced voxelized regularization in point cloud registration, applying spatial B-spline smoothing in voxelized 3D space to stabilize deep learning-based point cloud registration, though this voxelized concept has not been used in optimization-based point cloud registration. Their work also does not consider explicit biomechanical energy regularization, which is necessary for medical point cloud registration.

B. Contributions

In this paper, we propose a new point-matching-based registration method for medical point cloud registration that addresses the lack of semantic information and biomechanical energy regularization. We first propose using semantic labels in the point-matching step, then introduce a novel deformation representation in point clouds and explicit biomechanical energy regularization into point cloud registration. The method was tested on three entirely different datasets and achieved the best surface matching performance compared with other point-matching-based registration algorithms. To the best of our knowledge, our contributions include: (1) the first work to systematically use semantic labels for non-rigid point cloud alignment; (2) the first work to use explicit biomechanical energy regularization in point cloud registration; (3) validation of the effectiveness of (1) and (2) in medical point clouds, with a fixed set of hyperparameters that underwent minimal tuning. The rest of this paper is organized as follows. Section II describes the proposed method, and Section III presents validation results on three datasets, ablation studies, and sensitivity analyses. Section IV provides the discussion.

II. METHODS

We define the source point cloud as $P = \{p_0, p_1, \dots, p_N\}$ and the target as $Q = \{q_0, q_1, \dots, q_M\}$, with the points $p, q \in \mathbb{R}^3$. The point clouds are associated with semantic labels $L_p = \{x_0, x_1, \dots, x_N\}$ and $L_q = \{y_0, y_1, \dots, y_M\}$. The labels belong to the label set $L = \{l_1, l_2, \dots, l_K\}$, where K is the number of labels. We assume that the observed points have at least two labels, $K \geq 2$. Apart from the 3D location of the points, the point clouds also have local normals at each point: $N_p = \{n_0, \dots, n_N\}$, $N_q = \{m_0, \dots, m_M\}$. The local normals can be estimated using surface reconstruction methods such as ball pivoting [36]. The registration workflow of Semantic-ICP (SemiICP), is shown in Fig. 1; it first estimates a rigid transform $T \in SE(3)$, then refines it by non-rigid registration.

A. Rigid Initialization

The optimal rigid transform $T \in SE(3)$ is iteratively estimated by minimizing a cost function that measures the difference between point clouds, as described in Algorithm 1. SemiICP uses the semantic information during point pair

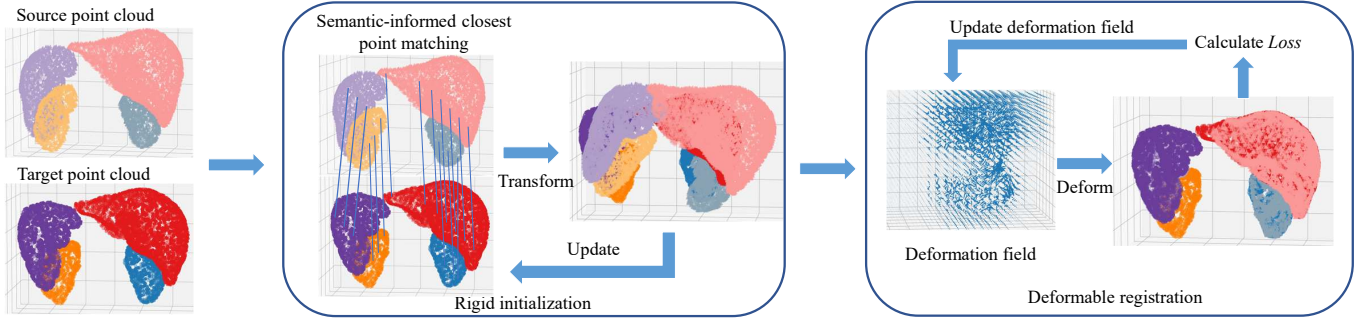


Fig. 1. The workflow of our proposed Sem-ICP. The method includes a rigid initialization, and then the deformation is estimated iteratively.

matching, such that matched point pairs have the same semantic labels. At each iteration i , for each point p_j from P , we find the closest point q_j in Q that has the smallest L2 distance with the same semantic label as p_j . KD-tree is used to accelerate the search for matched point pairs. The update value ΔT^i is automatically estimated using the autograd function in PyTorch. We use an Adam optimizer [37] to minimize the cost function L_{rigid} that measures the point-to-plane distance [38] of matched point pairs at each iteration:

$$L_{rigid} = \sum_{j=1}^N |(Rp_j^i + t - q_j^i) \cdot m_j|, \quad (1)$$

t is the translation and R is the rotation of the rigid transformation T between the two point clouds. R is parametrized by XYZ Euler angles. m_j is the local normal of point p_j , and the cost function measures the error along the surface normal. Compared with point-to-point L2 distance, point-to-plane distance encourages the matched points to be on the same plane instead of being strictly aligned. The matched point pairs are recomputed at each iteration with the updated source point cloud. The iteration is repeated until L_{rigid} is no longer improved or the maximum number of iterations is reached.

Algorithm 1 Rigid initialization

Input: Source point cloud P and target point cloud Q .

Output: Optimal rigid transformation T .

```

1: Initialization:  $T^0 = I, P^0 = P$ .
2: for  $i = 0$  to  $max\_iter - 1$  do
3:   for  $l \in L$  do
4:     Point sets  $P_{sub}^i, Q_{sub}$  with the same label  $l$ .
5:     for  $p_j^i$  in  $P_{sub}^i$  do
6:       Acquire matched  $q_j^i$  with smallest L2 distance.
7:     end for
8:   end for
9:    $\Delta T^i \leftarrow \arg \min L_{rigid}(T^i)$ 
10:   $T^{i+1} \leftarrow \Delta T^i + T^i, P^{i+1} \leftarrow \Delta T^i P^i$ 
11:  if Converge then
12:    break
13:  end if
14: end for
15: return  $T^{final}$ 

```

B. Non-rigid Registration

Non-rigid registration is performed after the initial rigid alignment. The non-rigid registration estimates the deformation field D that deforms the source point cloud P to be aligned with the target Q . Instead of parameterizing the deformation D as the movement at each surface point p , we uniformly sample N_C control points $C = \{c_i = (x_1^i, x_2^i, x_3^i), i = 1, 2, \dots, N_C\}$ in the point cloud bounding box, and use the deformation d_c at these control points to describe the deformation field $D \in \mathbb{R}^{N_C \times 3}$, where $D(i) = d_{c_i}$. Our new point cloud deformation field representation provides several improvements over the state of the art. First, the control point-based representation is more consistent in memory usage since it does not depend on the density of the input point clouds. Second, the individual point movement is more regularized because it is interpolated from neighboring control points. Last but not least, this new deformation representation enables *explicit* biomechanics-based regularization, since it also models the inner tissue deformation rather than only describing the boundary conditions.

The deformation is iteratively estimated, as shown in Algorithm 2. In each iteration i , we use the same label-informed nearest point matching method employed earlier during rigid initialization to find the matched point pair (p_j^i, q_j^i) , and use the Adam optimizer to minimize the loss:

$$L_{non-rigid}(D) = \sum_{j=1}^N \|p_j^i + d_j^i - q_j^i\|_2 + Reg(D) \quad (2)$$

d_j is the surface point deformation at point p_j . We compute d_j using a trilinear interpolation of the deformation at the control points that are in p 's neighborhood.

$$d_j = \text{interpolate}(d_{c_1}, \dots, d_{c_n}), \{c_1, \dots, c_n\} = \text{Neighbor}(p_j) \quad (3)$$

The first term in (2) minimizes the distance between the matched point pairs, while the remaining regularization term controls tissue deformation. The regularization term includes elastic energy Reg_{els} , deformation magnitude Reg_{mag} and the smoothness of deformation field Reg_{grad} :

$$Reg(D) = \alpha Reg_{els}(D) + \beta Reg_{mag}(D) + \gamma Reg_{grad}(D) \quad (4)$$

We use linear elastic regularization [33], [39] to regularize the deformation. In continuum mechanics, the linear elastic energy can be described using the Navier-Lamé Equation. We

approximate the Navier-Lamé Equation with the numerical differentiation at the control points and add a scaling factor to normalize the energy, where Δ is the step size of the control points.

$$Reg_{els}(\mathbf{D}) = \frac{\Delta}{N_C} \sum_c \left(\frac{\mu}{4} \sum_{j=1}^3 \sum_{k=1}^3 \left(\frac{\partial \mathbf{D}_j}{\partial x_k} + \frac{\partial \mathbf{D}_k}{\partial x_j} \right) + \frac{\lambda}{2} (\nabla \mathbf{D})^2 \right) \quad (5)$$

We use a two-point estimation for numerical differentiation:

$$\frac{\partial \mathbf{D}_i}{\partial x_j} = \frac{\mathbf{D}(x_j + \Delta, i) - \mathbf{D}(x_j, i)}{\Delta}, \quad \nabla \mathbf{D} = \sum_{i=1}^3 \frac{\partial \mathbf{D}_i}{\partial x_i} \quad (6)$$

λ and μ are Lamé parameters, which can be estimated based on Young's modulus E and Poisson's ratio ν :

$$\lambda = \frac{E\nu}{(1+\nu)(1-2\nu)}, \quad \mu = \frac{E}{2(1+\nu)} \quad (7)$$

In addition to the above energy regularization, the regularization term also includes magnitude regularization Reg_{mag} to reduce unwanted large deformation, and a gradient regularization Reg_{grad} to encourage control grid smoothness:

$$Reg_{mag}(\mathbf{D}) = \frac{1}{N_C} \sum_i^{N_C} \|\mathbf{c}_i\|_2 \quad (8)$$

$$Reg_{grad}(\mathbf{D}) = \frac{\Delta}{N_C} \sum_c \left\| \frac{\partial \mathbf{D}}{\partial x_1} \right\|_2 + \left\| \frac{\partial \mathbf{D}}{\partial x_2} \right\|_2 + \left\| \frac{\partial \mathbf{D}}{\partial x_3} \right\|_2 \quad (9)$$

Algorithm 2 Non-rigid refinement

Input: Source point cloud P and target point cloud Q .

Output: Optimal deformation field \mathbf{D} .

```

1: Initialization:  $\mathbf{D}^0 = \mathbf{0}$ .
2: for  $i = 0$  to  $max\_iter - 1$  do
3:   for  $j \in N$  do
4:      $\mathbf{d}_j^i = \text{interp}(\mathbf{D}^i)$  at  $\mathbf{p}_j$ ,  $\mathbf{p}_j^i = \mathbf{p}_j + \mathbf{d}_j^i$ 
5:   end for
6:   Find point pairs  $(\mathbf{p}_j^i, \mathbf{q}_j^i)$  (line 3-8 in Algorithm 1)
7:    $\Delta \mathbf{D}^i \leftarrow \arg \min L_{non-rigid}(\mathbf{D}^i)$ 
8:    $\mathbf{D}^{i+1} \leftarrow \Delta \mathbf{D}^i + \mathbf{D}^i$ 
9:   if Converge then
10:    break
11:   end if
12: end for
13: return  $\mathbf{D}^{final}$ 
```

III. EXPERIMENTS AND RESULTS

A. Datasets

The experiments are performed on one private dataset derived from trans-oral robotic surgery (TORS), and two public datasets from Learn2Reg challenges [40]. We use the training data in the Learn2Reg challenges, since label maps for test

data are not included in the public dataset link¹. 3D slicer is used to extract point clouds from the label maps [41].

TORS: This dataset contains 3D freehand US and CT images of the neck collected from patients who underwent TORS for oral cancer between January 2022 and November 2024 at the Vancouver General Hospital (Vancouver, BC, Canada). This study received ethics approval from the University of British Columbia Clinical Research Ethics Board (H19-04025). Informed consent was obtained from all participants included in this study. The procedures used in this study adhere to the tenets of the Declaration of Helsinki. Diagnostic CT data were collected preoperatively, and US data were collected before surgery while patients were anesthetized. A BK3500 with a 14L3 linear 2D transducer (BK Medical, Burlington, MA) and a Polaris Spectra (Northern Digital, ON, Canada) were used to collect freehand 3D US. PLUS [42] was used to calibrate the US probe and collect tracked US data. The image depth was set to 4 or 5 cm (depending on patient anatomy) at 9 MHz, and US imaging was carried out ipsilateral to the tumor. A medical student and an experienced research assistant labeled the carotid artery, jugular vein, and larynx/mandibular bone in 2D US frames and CT volumes, then the 2D US label maps were reconstructed in 3D. The dataset contains 24 pairs of US-CT images from 12 patients. The bifurcation point and the axis of the carotid in US and CT were used to pre-align volumes.

AbdominalMRCT [43]: The Learn2reg dataset contains 8 pairs of intra-patient abdominal magnetic resonance (MR) and CT images. The label maps include 3D segmentation of 4 anatomical labels of liver, spleen, right kidney and left kidney.

HippocampusMR [44]: The Learn2reg challenge dataset includes MR images from 90 healthy adults and 105 adults with a non-affective psychotic disorder, along with segmentations of the head and body of the hippocampus. We use the validation registration pairs provided in the dataset's JSON files, resulting in 60 inter-patient registration pairs.

B. Compared Baselines

We compare our method with established rigid and non-rigid point-matching-based point cloud registration methods. The baseline methods include the original ICP [6], Global-ICP (GO-ICP) [13], Fast-robust-ICP (FR-ICP) [14], non-rigid ICP (NR-ICP) [10], Fast-RNRR [11] and AMM-NRR [12]. We used the default parameters provided in the baselines' open-source codes. To evaluate the point cloud surface similarity, we use the 95th percentile of the Hausdorff Distance (HD95) and the mean surface distance (MSD) to determine the surface differences between the source and target point clouds.

$$HD95(P, Q) = Pct95_{p \in P} \left(\min_{q \in Q} \|\mathbf{p} - \mathbf{q}\|_2 \right) \quad (10)$$

$$MSD(P, Q) = \frac{1}{N_P} \sum_{p \in P} \left(\min_{q \in Q} \|\mathbf{p} - \mathbf{q}\|_2 \right) \quad (11)$$

¹<https://learn2reg.grand-challenge.org/Datasets/>

In the synthetic sensitivity study, we also report the average target registration error (TRE).

$$TRE(P, Q) = \frac{1}{N_p} \sum_{p \in P} \|p - q\|_2 \quad (12)$$

To evaluate the deformation field's topology, we report the standard deviation of the logarithmic Jacobian determinant (SDLogJ) that measures spatial distortion.

C. Implementation Details

The methods were implemented with a 12GB Nvidia GeForce RTX 3060 GPU, using Python 3.9.18, PyTorch 2.1.2, and CUDA-11.8. In the rigid initialization, the learning rate of the optimizer is 0.001 and the maximum number of iterations is 1000. For non-rigid refinement, the learning rate is 0.01, and the maximum number of iterations is 300. The optimization will be stopped early when the loss is no longer improved. Each point's coordinate was normalized to $[0,1]$ for better convergence, and we uniformly sampled $25 \times 25 \times 25$ control points in the $[0,1]^3$ space. The resulting spacing of the control grids for three datasets are: 2.04 mm \times 2.43 mm \times 3.66 mm for TORS dataset, 12.78 mm \times 8.88 mm \times 10.03 mm for AbdominalMRCT dataset, and 0.97 mm \times 1.69 mm \times 1.11 mm for HippocampusMR dataset. We assume that all the tissues have a Young's modulus of $E = 1\text{kPa}$ [45] and are almost incompressible, with a Poisson's ratio of $\nu = 0.499$. The codes will be made public, accompanying the published paper.

D. Evaluation on Datasets

We report the quantitative evaluation using HD95 and MSD across three datasets, as shown in Tables I to VI. Compared to other baselines, our method SemICP achieves the lowest HD95 and MSD for each anatomical structure, as well as the lowest average across labels, on all three datasets.

TORS: The quantitative results are shown in Table I and II. AMM-NRR and Fast-RNRR completed registration on only 7 pairs of 24 data pairs, with numerical issues affecting the remaining data. One Fast-RNRR result was highly inaccurate and is treated as a failed registration, not included in the final analysis. One unique challenge associated with this dataset is that the US provides only partial observation of relevant anatomical structures, especially the larynx and bony structures, resulting in differing point cloud sizes between US and CT. Additionally, visibility varies across anatomical structures. Our results show that other registration methods have larger HD95 and MSD when registering all anatomical structures, especially the larynx and bony structures. Without semantic information, other non-rigid registration algorithms under-penalize the larynx/bone registration error. Mismatching different structures also occurs in other baselines without semantic information, as shown in the qualitative evaluation in Fig. 2. Our method improves the delineation of anatomical structures and leads to significantly lower HD95 and MSD across all labels, greatly improving registration accuracy.

AbdominalMRCT: Table III and IV show and HD95 and MSD on this dataset. Results for AMM-NRR and Fast-RNRR

are reported on only 7 MR-CT pairs due to a numerical problem encountered with one point cloud pair. The challenge of this dataset is that the organs undergo significant deformation, so all rigid registration methods have a relatively large surface distance as shown in Fig. 3. Our method achieves the lowest surface distance for all organs compared to baseline methods.

HippocampusMR: HD95 and MSD results are reported in Table V and Table VI, respectively. This dataset includes only the head and tail of the hippocampus, which are relatively small structures with limited deformation compared to abdominal organs. While other non-rigid methods also achieve sub-millimeter HD95 and MSD, our method SemICP yields the lowest distance errors. AMM-NRR and Fast-RNRR completed registration on 58 pairs, with two pairs excluded due to numerical issues while building the deformation graph and sampling the influencing node sets.

E. Ablation Studies

We perform two different experiments to evaluate the effect of label consistency constraints and elastic energy regularization. The experiments are performed on the AbdominalMRCT dataset. We switch off the label consistency constraints in SemICP while keeping the regularizations (W/o semantic matching + *Reg*). In the point matching step, the points from the source point cloud will be matched to the closest points in the target point cloud, without requiring that the label of the points be consistent. We also evaluate the proposed elastic energy regularization by performing SemICP with different combinations of the regularization terms.

The results of these two experiments are shown in Table VII. Comparing W/o semantic matching + *Reg* and Semantic + *Reg*, both HD95 and MSD are improved with semantic-informed matching. As shown in Fig. 5(a), the absence of semantic consistency leads SemICP to predict anatomically implausible boundaries due to organ mismatches. Table VII also shows that the deformation field without any regularization (Semantic w/o *Reg*) has the highest SDLogJ, indicating significant distortion. Among the individual regularization terms (Semantic + *Reg_{grad}*, Semantic + *Reg_{mag}*, Semantic + *Reg_{els}*), Semantic + *Reg_{els}* achieves the lowest SDLogJ while maintaining comparable HD95 and MSD. This suggests that *Reg_{els}* best preserves deformation topology without sacrificing surface distance accuracy. It also outperforms *Reg_{grad}* in maintaining deformation smoothness. Fig. 5(b) also shows that our regularization generates a smoother deformation map.

F. Sensitivity on Elasticity Values

To evaluate the sensitivity of our method to the Young's modulus E and Poisson's ratio ν , we perform SemICP on the AbdominalMRCT dataset with varying elastic values. Based on finite element simulation [46], typical E for soft tissues and abdominal organs ranges from 1kPa to 100 kPa, except only the stomach that reaches 500kPa, and ν typically ranges from 0.400 to 0.499. In E sensitivity analysis, we fixed $\nu = 0.499$ and varied E across $\{1\text{kPa}, 10\text{kPa}, 100\text{kPa}, 500\text{kPa}, 1\text{MPa}\}$. To also understand the influence of ν , we fixed E at 1kPa and varied ν in $\{0.350, 0.400, 0.450, 0.499\}$.

TABLE I

THE AVERAGE HD95 ON THE TORS DATASET. THE METRICS ARE REPORTED IN MEAN (STD) IN *mm* AND THE BEST PERFORMANCE IS HIGHLIGHTED IN BOLD.

	Initial	ICP	GO-ICP	FR-ICP	SemICP-rigid	nr-ICP	AMM-NRR	Fast-RNRR	SemICP
Carotid	5.47 ± 2.68	9.63 ± 5.18	5.68 ± 3.47	7.84 ± 4.95	4.59 ± 2.52	9.12 ± 5.78	17.4 ± 0.40	3.01 ± 1.58	0.61 ± 0.17
Larynx/bone	10.21 ± 9.27	8.07 ± 8.44	7.20 ± 9.04	7.78 ± 8.92	7.18 ± 8.62	5.57 ± 9.43	4.10 ± 3.24	5.92 ± 5.08	1.12 ± 2.18
Vein	10.85 ± 4.29	7.24 ± 5.22	5.47 ± 3.01	7.17 ± 5.69	5.38 ± 2.62	6.38 ± 6.08	3.08 ± 0.72	6.53 ± 5.12	0.68 ± 0.37
Average	8.84	8.31	6.12	7.60	5.72	7.02	2.97	5.15	0.80

TABLE II

THE AVERAGE MSD ON THE TORS DATASET. THE METRICS ARE REPORTED IN MEAN (STD) IN *mm* AND THE BEST PERFORMANCE IS HIGHLIGHTED IN BOLD.

	Initial	ICP	GO-ICP	FR-ICP	SemICP-rigid	nr-ICP	AMM-NRR	Fast-RNRR	SemICP
Carotid	2.19 ± 0.92	4.02 ± 2.61	2.07 ± 1.08	2.87 ± 1.83	1.86 ± 0.92	3.55 ± 2.91	0.71 ± 0.10	1.25 ± 0.66	0.30 ± 0.05
Larynx/bone	4.72 ± 4.26	3.44 ± 5.29	3.23 ± 5.41	3.40 ± 5.68	3.07 ± 4.78	2.47 ± 5.59	1.70 ± 2.16	2.74 ± 3.34	0.34 ± 0.29
Vein	5.25 ± 2.52	3.37 ± 2.64	2.39 ± 1.46	2.93 ± 2.31	2.37 ± 1.28	2.65 ± 3.01	0.93 ± 0.12	3.09 ± 2.44	0.32 ± 0.09
Average	4.05	3.61	2.56	3.07	2.43	2.89	1.11	2.36	0.32

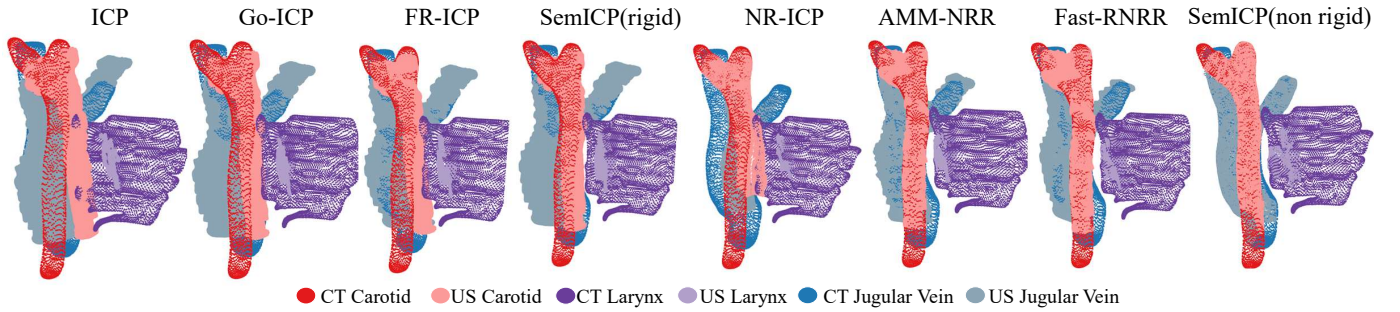


Fig. 2. Visualization of the registration results on one example US-CT pair in TORS dataset (posterior-anterior view).

TABLE III

THE AVERAGE HD95 ON THE LEARN2REG ABDOMINALMRCT. THE METRICS ARE REPORTED IN MEAN (STD) IN *mm* AND THE BEST PERFORMANCE IS HIGHLIGHTED IN BOLD.

	Initial	ICP	GO-ICP	FR-ICP	SemICP-rigid	nr-ICP	AMM-NRR	Fast-RNRR	SemICP
Liver	38.07 ± 14.60	19.20 ± 5.96	18.82 ± 5.74	26.35 ± 10.78	19.14 ± 5.78	4.02 ± 3.52	6.05 ± 2.25	16.95 ± 17.57	1.12 ± 0.14
Spleen	37.12 ± 17.25	16.89 ± 5.78	16.06 ± 6.08	24.29 ± 11.60	16.73 ± 5.58	3.55 ± 3.39	6.87 ± 4.58	10.45 ± 13.59	1.06 ± 0.05
Kidney-R	34.41 ± 20.42	15.04 ± 7.06	15.24 ± 6.49	14.59 ± 7.86	14.56 ± 6.95	3.98 ± 3.70	22.20 ± 27.03	18.55 ± 20.74	1.19 ± 0.15
Kidney-L	33.15 ± 14.37	20.80 ± 9.24	21.13 ± 9.65	22.70 ± 10.06	21.17 ± 9.80	5.66 ± 3.74	17.71 ± 17.01	12.68 ± 12.85	1.32 ± 0.21
Average	35.69	17.98	17.81	21.98	17.90	4.30	13.21	14.66	1.17

TABLE IV

THE AVERAGE MSD ON THE LEARN2REG ABDOMINALMRCT. THE METRICS ARE REPORTED IN MEAN (STD) IN *mm* AND THE BEST PERFORMANCE IS HIGHLIGHTED IN BOLD.

	Initial	ICP	GO-ICP	FR-ICP	SemICP-rigid	nr-ICP	AMM-NRR	Fast-RNRR	SemICP
Liver	18.22 ± 7.00	8.31 ± 3.39	8.14 ± 3.20	9.07 ± 3.82	8.15 ± 3.26	1.73 ± 1.41	2.00 ± 0.69	6.86 ± 8.61	0.64 ± 0.05
Spleen	18.22 ± 11.84	7.36 ± 2.51	7.26 ± 2.72	9.65 ± 5.52	7.62 ± 2.62	1.49 ± 1.13	2.33 ± 1.35	4.71 ± 6.83	0.63 ± 0.03
Kidney-R	17.05 ± 12.99	6.83 ± 3.59	6.82 ± 3.14	5.64 ± 2.66	6.48 ± 3.21	1.71 ± 1.59	10.88 ± 17.96	9.26 ± 12.39	0.69 ± 0.06
Kidney-L	14.32 ± 6.04	8.86 ± 4.05	8.98 ± 4.05	8.69 ± 4.46	8.83 ± 4.01	2.25 ± 1.59	4.84 ± 4.16	5.01 ± 5.80	0.73 ± 0.05
Average	16.95	7.84	7.80	8.26	7.77	1.80	5.01	6.46	0.67

TABLE V

THE AVERAGE HD95 ON THE LEARN2REG HIPPOCAMPUSMR. THE METRICS ARE REPORTED IN MEAN (STD) IN *mm*.

	Initial	ICP	GO-ICP	FR-ICP	SemICP-rigid	nr-ICP	AMM-NRR	Fast-RNRR	SemICP
Head	3.68 ± 1.46	2.44 ± 1.05	2.46 ± 1.12	2.84 ± 1.43	2.34 ± 0.90	0.85 ± 0.76	0.85 ± 0.76	2.61 ± 1.60	0.28 ± 0.03
Tail	3.68 ± 1.23	2.23 ± 0.97	2.21 ± 1.06	2.46 ± 1.29	1.97 ± 0.79	0.82 ± 0.75	0.82 ± 0.75	2.12 ± 1.45	0.28 ± 0.02
Average	3.68	2.33	2.33	2.64	2.16	0.84	0.84	2.36	0.28

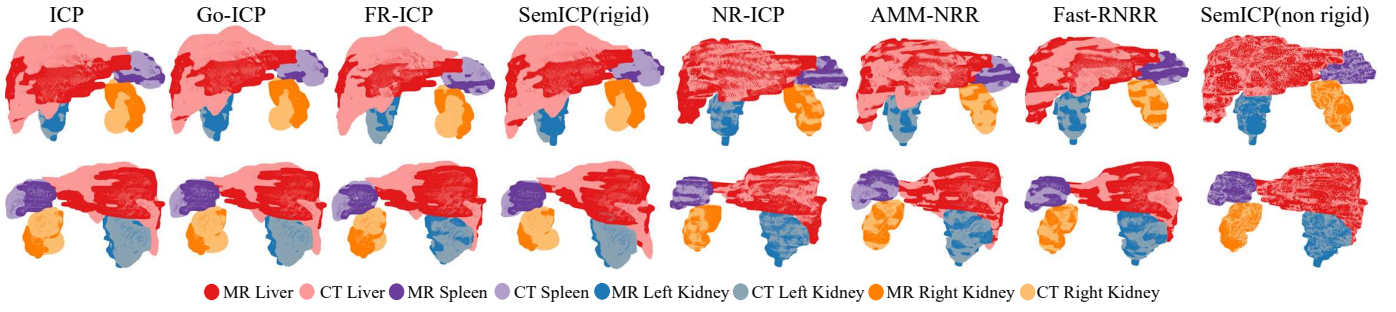


Fig. 3. Visualization of the registration results on one example CT-MR pair in AbdominalMRCT dataset. The first row is the anterior-posterior view, and the second row is the posterior-anterior view.

TABLE VI

THE AVERAGE MSD ON THE LEARN2REG HIPPOCAMPUSMR. THE METRICS ARE REPORTED IN MEAN (STD) IN *mm*.

	Initial	ICP	GO-ICP	FR-ICP	SemICP-rigid	nr-ICP	AMM-NRR	Fast-RNRR	SemICP
Head	1.73 ± 0.73	1.04 ± 0.36	1.04 ± 0.37	1.09 ± 0.47	1.03 ± 0.34	0.40 ± 0.21	0.40 ± 0.21	0.95 ± 0.50	0.12 ± 0.02
Tail	1.60 ± 0.48	0.94 ± 0.29	0.93 ± 0.31	0.91 ± 0.31	0.88 ± 0.26	0.40 ± 0.23	0.40 ± 0.23	0.76 ± 0.31	0.12 ± 0.01
Average	1.67	0.99	0.98	1.00	0.95	0.40	0.40	0.85	0.12

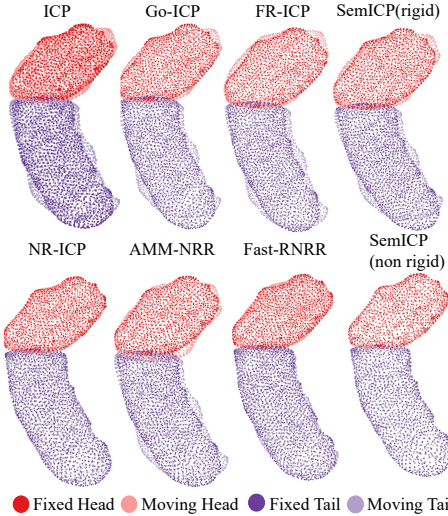


Fig. 4. Visualization of the registration results on one example MR-MR pair in HippocampusMR dataset (superior-inferior view).

TABLE VII

ABLATION STUDIES ON WITH SEMANTIC-INFORMED MATCHING AND REGULARIZATION TERMS. HD95 AND MSD ARE REPORTED IN *mm*. THE BEST VALUES ARE BOLD AND THE SECOND BEST IS UNDERLINED. * MEANS THE THE RESULTS IS SIGNIFICANT DIFFERENCE COMPARED WITH SEMANTIC + *Reg* UNDER $p \leq 0.05$ IN A TWO-SAMPLE T-TEST.

	HD95 ↓	MSD ↓	SDLogJ ↓
Initial	35.69	16.95	N/A
W/o semantic matching + <i>Reg</i>	2.42*	0.90*	0.0025
Semantic w/o <i>Reg</i>	1.15*	0.66*	0.12*
Semantic + <i>Reg_{grad}</i>	1.15*	0.66*	0.0045*
Semantic + <i>Reg_{mag}</i>	1.15*	0.66*	0.0089*
Semantic + <i>Reg_{els}</i>	<u>1.17</u>	<u>0.67</u>	<u>0.0025</u>
Semantic + <i>Reg_{grad}</i> + <i>Reg_{mag}</i>	1.15*	0.66*	0.0045*
Semantic + <i>Reg_{grad}</i> + <i>Reg_{els}</i>	<u>1.17</u>	<u>0.67</u>	0.0024
Semantic + <i>Reg_{mag}</i> + <i>Reg_{els}</i>	1.15	<u>0.67</u>	0.0025
Semantic + <i>Reg</i> (Ours)	<u>1.17</u>	<u>0.67</u>	<u>0.0025</u>

TABLE VIII

THE AVERAGE HD95, MSD AND SDLOGJ OF ALL LABELS FOR DIFFERENT YOUNG'S MODULUS E , WHILE $\nu = 0.499$. HD95 AND MSD ARE REPORTED IN *mm*. * MEANS THE RESULTS ARE SIGNIFICANTLY DIFFERENT COMPARED WITH $E=1$ KPa UNDER $p \leq 0.05$ IN A TWO-SAMPLE T-TEST.

E	1kPa	10kPa	100kPa	500kPa	1MPa
HD95 ↓	1.17	1.20*	1.23*	1.49*	1.85*
MSD ↓	0.67	0.68*	0.71*	0.81*	0.91*
SDLogJ ↓	0.0025	0.0018*	0.0011*	0.0008*	0.0008*

The sensitivity of SemICP to E is presented in Table VIII. As Young's modulus E increases, the surface matching errors HD95 and MSD increase slightly, while the spatial distortion SDLogJ decreases. However, the absolute differences across metrics remain small, particularly between 1kPa and 100kPa. The results indicate that as the tissue stiffness increases, the estimated deformation becomes more regularized, but its ability to accurately fit the boundary conditions slightly diminishes. However, in the soft tissues and soft organs range, the differences in performance are small. The sensitivity of SemICP to Poisson's Ratio ν is shown in Table IX. The surface matching has a slight improvement when the ν decreases, while the spatial distortion SDLogJ increases. It indicates that assuming greater tissue compressibility weakens the linear energy regularization, allowing larger but less regularized deformations to fit the boundary conditions. Nonetheless, the differences in metrics remain small.

G. Sensitivity on Misalignment and Visualizable Ratio

To assess the sensitivity of our method and its robustness with respect to initial misalignments, we simulated partial observations and applied different rigid misalignments to the AbdominalMRCT dataset. We cropped the original point clouds to partially visible point clouds with 5%, 10%, 25%

TABLE IX

THE AVERAGE HD95, MSD AND SDLogJ OF ALL LABELS FOR DIFFERENT POISSON'S RATIO ν , WITH $E=1\text{kPa}$. HD95 AND MSD ARE REPORTED IN *mm*. * MEANS THE RESULTS ARE SIGNIFICANTLY DIFFERENT COMPARED WITH $\nu = 0.499$ UNDER $p \leq 0.05$ IN A TWO-SAMPLE T-TEST.

ν	0.350	0.400	0.450	0.499
HD95 ↓	1.16*	1.16	1.16*	1.17
MSD ↓	0.66*	0.66*	0.66*	0.67
SDLogJ ↓	0.0039*	0.0038*	0.0037*	0.0025

and 50% of points visible, and introduced additional Gaussian noise. We also added different levels of misalignment, with Euler rotation angles within $\pm 5^\circ$, $\pm 15^\circ$, and $\pm 30^\circ$. For each experiment, we generated 10 different simulated partial point clouds for each patient, resulting in a total of 80 synthetic point cloud pairs. We compare our SemICP-rigid method with ICP and GO-ICP. FR-ICP is excluded from comparison due to its higher HD95 in Table III, indicating less favorable performance. As shown in Table X, SemICP-rigid achieves lower HD95, MSD, and TRE compared to ICP and GO-ICP under challenging visibility conditions (5%, 10%, and 25%). When evaluating sensitivity to initial misalignment, both ICP and GO-ICP exhibit significantly increased registration error at rotation angles of $\pm 30^\circ$, indicating sensitivity to initialization. In contrast, SemICP-rigid demonstrates improved robustness, with smaller error increases under the same conditions. These results highlight that incorporating semantic labels enhances the accuracy and stability of the rigid registration step, even under limited visibility and challenging initial alignment.

IV. DISCUSSION

The datasets in our evaluation present different challenges. The TORS dataset features partial point cloud registration and suffers from severe class imbalance, making consistent registration difficult. AbdominalMRCT has large displacements between point clouds. HippocampusMR, on the other hand, features small structures, requiring precise, fine-scale registration. Our method improves the delineation of anatomical structures and consistently achieves lower HD95 and MSD values compared to existing approaches, highlighting the strength of our proposed method. Our non-rigid registration method, which crucially involves the use of semantic labeling in point matching, greatly improved registration accuracy. Label-informed matching effectively reduces mismatches that are commonly encountered in traditional point-matching-based methods, and the ablation study demonstrates that without semantic matching in SemICP, the HD95 and MSD increase. Overall, our findings show that incorporating semantic context into the registration pipeline substantially improves accuracy and anatomical plausibility across a wide range of scenarios. The sensitivity study further demonstrates that the semantic context can improve the rigid initialization in challenging scenarios, including low visibility and large initial misalignment.

Our work introduces a novel biomechanical energy-based regularization into point-matching-based point cloud registration. Existing methods (NR-ICP, AMM-NRR and Fast-RNRR)

regularize the deformation with a local affine regularization to constrain deformation, which fails to capture the underlying biomechanical properties of medical point clouds. Moreover, these methods focus solely on surface matching, neglecting the fact that medical point clouds often undergo deformation as cohesive volumetric structures. This limits their ability to assess and preserve the underlying deformation topology. Our elastic energy-based regularization is physically motivated by the biomechanical properties of anatomical structures and may explain why it works better. Ablation studies confirm that the inclusion of the proposed elastic energy regularization leads to significant improvements in the plausibility and quality of the estimated deformation fields, as evidenced by reduced SD-LogJ, with little degradation in the surface matching accuracy.

We do not apply the actual elasticity values in the regularization, but the sensitivity studies show that the differences in HD95, MSD and SDLogJ remain small with various E and ν . The non-rigid cost function includes two parts: the first part is boundary conditions that drive the alignment of the organ surfaces, and the second part is regularization that includes elastic energy. They work together to reach the equilibrium between accuracy and smoothness. Our sensitivity experiments on E show that the registration is more likely to be driven by boundary conditions than by the regularization, particularly when E is within the range of 1kPa to 100kPa, including the soft organs of interest like liver and kidney [47] and brain [48]. Similar results are observed in finite element-based registration. Chi et al. [49] found that a 30% material uncertainty results in registration errors within 1.3mm for thin and hollow structures, and though the maximum error for prostate can reach up to 4.5mm, most of the subvolumes have a much smaller registration error. Our sensitivity experiments on ν indicate that ν has a small influence on the registration results, which is similar to the finding in the finite element-based registration [46] that varying ν only leads to small changes in accuracy. In the future, inhomogeneous E and ν can be employed based on the labels or information from elastography [33]. More complicated non-linear effects might be integrated, but it requires the consideration of the trade-off between algorithm complexity and accuracy. A research in finite element-based lung registration shows that the registration error is not significantly affected by the element type (elastic and hyperelastic) or linearity of analysis, suggesting the use of linear finite element analysis for simplicity [50].

In our experiments, AMM-NRR and Fast-RNRR encountered numerical problems during the initialization phase of non-rigid registration on several samples. These issues arose during the construction of the deformation graph, where small and irregular triangle faces resulted in unstable edge angle computations. This sensitivity to mesh quality highlights a limitation of their approach: it relies on geometric assumptions that do not generalize well to real-world medical data, which often contains non-uniform, sparse, or noisy point distributions. As a result, their methods may fail or produce unreliable deformations when applied to anatomically complex point clouds, limiting their robustness in clinical scenarios.

Our work requires semantic labels in the point cloud, and this paper focuses on registration without discussing the

TABLE X

THE AVERAGE HD95, MSD AND TRE OF ALL LABELS FOR DIFFERENT RIGID ICP METHODS WITH VARIANT VISIBLE RATIOS OF THE POINT CLOUD. THE NUMBERS ARE REPORTED IN *mm*. THE BEST VALUES ARE BOLD AND THE SECOND BEST IS UNDERLINED. * MEANS THE RESULTS ARE SIGNIFICANTLY DIFFERENT COMPARED WITH THE BEST OR THE SECOND-BEST EXPERIMENTS UNDER $p \leq 0.05$ IN A TWO-SAMPLE T-TEST.

Vis	Rot	Init			ICP			GO-ICP			SemICP-rigid		
		HD95	MSD	TRE	HD95	MSD	TRE	HD95	MSD	TRE	HD95	MSD	TRE
5%	$\pm 5^\circ$	13.60	6.31	14.17	43.31	29.53	59.28	9.39	4.02	8.58	9.24*	3.94	8.23
	$\pm 15^\circ$	32.95	19.52	42.73	36.20	23.70	51.99	<u>12.09</u>	<u>5.85</u>	<u>14.20</u>	10.12*	4.34*	10.42*
	$\pm 30^\circ$	61.06	43.25	80.26	42.35	28.89	61.36	<u>27.97</u>	<u>18.15</u>	<u>40.61</u>	13.82*	6.27*	19.75*
10%	$\pm 5^\circ$	13.74	6.22	13.19	42.49	28.24	55.73	<u>9.27</u>	<u>3.96</u>	<u>8.35</u>	9.23	3.95	8.20
	$\pm 15^\circ$	30.90	17.45	38.22	35.83	23.23	47.19	<u>11.34</u>	<u>5.20</u>	<u>12.32</u>	10.19	4.41	10.10
	$\pm 30^\circ$	55.44	35.60	70.28	36.21	22.75	50.35	<u>23.59</u>	<u>13.28</u>	<u>32.00</u>	14.55*	6.44*	18.55*
25%	$\pm 5^\circ$	13.73	6.09	14.11	17.62	9.49	20.22	<u>9.38</u>	<u>3.98</u>	<u>8.30</u>	9.37*	3.97*	8.22*
	$\pm 15^\circ$	33.27	17.21	40.83	18.84	9.58	22.65	<u>10.53</u>	<u>4.48</u>	<u>10.16</u>	10.43	4.42	9.90
	$\pm 30^\circ$	65.49	41.65	78.72	18.43	<u>8.52</u>	23.26	<u>16.81</u>	8.88	<u>19.40</u>	15.41	6.74*	17.79
50%	$\pm 5^\circ$	14.92	6.49	14.99	9.77	4.13	8.62	<u>9.55</u>	<u>4.03</u>	<u>8.34</u>	9.54	4.03	8.31*
	$\pm 15^\circ$	33.74	16.19	38.32	11.16	4.70	10.26	10.82	4.54	9.78	<u>10.91*</u>	<u>4.58*</u>	<u>9.88</u>
	$\pm 30^\circ$	72.80	43.07	81.74	<u>14.02</u>	<u>5.84</u>	<u>13.89</u>	13.16	5.42	12.29	<u>16.70*</u>	<u>7.10*</u>	<u>18.05*</u>

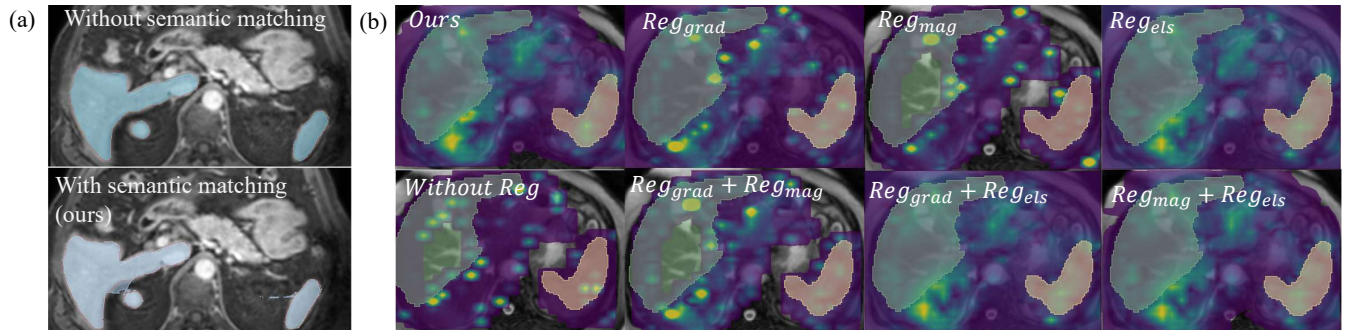


Fig. 5. (a) Comparison of SemICP with and without semantic matching. Top: Without semantic+Reg; Bottom: Semantic+Reg. (b) Comparison of different regularization terms. Yellow indicates larger deformation; green and orange masks represent the liver and spleen in CT segmentation.

point cloud labeling process. Preoperative images are often labeled manually, but intraoperative labeling can hinder real-time applications. In future work, we plan to investigate deep-learning models to perform intraoperative segmentation for the full registration pipeline. Additionally, this method is designed for multi-organ registration, but it has the potential to be generalized to single-organ registration as long as the point clouds have different semantic labels (such as using vessels inside the liver as additional labels). Finally, the homogeneous linear elastic energy is a simplified model, and future work can explore the use of different biomechanical parameters for different control points based on the type of tissue.

V. CONCLUSION

We present a novel non-rigid registration method that uses semantic label-based point matching to improve the quality of the matched point pairs. We utilize a novel control point-based deformation representation to enable explicit biomechanics-based regularization in point cloud registration. Our method outperforms state-of-the-art point matching-based registration methods on three different datasets, showing that it is generalizable to different tasks and challenges.

REFERENCES

- [1] L. Ma, T. Huang, J. Wang, and H. Liao, "Visualization, registration and tracking techniques for augmented reality guided surgery: a review," *Physics in Medicine & Biology*, vol. 68, no. 4, p. 04TR02, 2023.
- [2] Y. Wang and J. M. Solomon, "Deep closest point: Learning representations for point cloud registration," in *Proceedings of the IEEE/CVF international conference on computer vision (ICCV)*, 2019, pp. 3523–3532.
- [3] F. Poiesi and D. Boscaini, "Learning general and distinctive 3d local deep descriptors for point cloud registration," *IEEE Transactions on Pattern Analysis and Machine Intelligence*, vol. 45, no. 3, pp. 3979–3985, 2022.
- [4] M. Weber, D. Wild, J. Kleesiek, J. Egger, and C. Gsaxner, "Deep learning-based point cloud registration for augmented reality-guided surgery," in *2024 IEEE International Symposium on Biomedical Imaging (ISBI)*. IEEE, 2024, pp. 1–5.
- [5] Y. Zhang, Y. Zou, and P. X. Liu, "Point cloud registration in laparoscopic liver surgery using keypoint correspondence registration network," *IEEE Transactions on Medical Imaging*, vol. 44, no. 2, pp. 749–760, 2024.
- [6] P. J. Besl and N. D. McKay, "Method for registration of 3-d shapes," in *Sensor fusion IV: control paradigms and data structures*, vol. 1611. SPIE, 1992, pp. 586–606.
- [7] F. Liebmann *et al.*, "Automatic registration with continuous pose updates for marker-less surgical navigation in spine surgery," *Medical Image Analysis*, vol. 91, p. 103027, 2024.
- [8] M. Bayrak, A. Alsadoon, P. Prasad, H. S. Venkata, R. S. Ali, and S. Haddad, "A novel rotation invariant and manhattan metric-based pose refinement: Augmented reality-based oral and maxillofacial surgery," *The International Journal of Medical Robotics and Computer Assisted Surgery*, vol. 16, no. 3, p. e2077, 2020.
- [9] A. Myronenko and X. Song, "Point set registration: Coherent point drift," *IEEE transactions on pattern analysis and machine intelligence*, vol. 32, no. 12, pp. 2262–2275, 2010.
- [10] B. Amberg, S. Romdhani, and T. Vetter, "Optimal step nonrigid icp algorithms for surface registration," in *2007 IEEE conference on computer vision and pattern recognition (CVPR)*. IEEE, 2007, pp. 1–8.
- [11] Y. Yao, B. Deng, W. Xu, and J. Zhang, "Quasi-newton solver for robust

- non-rigid registration,” in *2020 IEEE/CVF Conference on Computer Vision and Pattern Recognition (CVPR)*, 2020, pp. 7597–7606.
- [12] —, “Fast and robust non-rigid registration using accelerated majorization-minimization,” *IEEE Transactions on Pattern Analysis and Machine Intelligence*, vol. 45, no. 8, pp. 9681–9698, 2023.
- [13] J. Yang, H. Li, D. Campbell, and Y. Jia, “Go-icp: A globally optimal solution to 3d icp point-set registration,” *IEEE transactions on pattern analysis and machine intelligence*, vol. 38, no. 11, pp. 2241–2254, 2015.
- [14] J. Zhang, Y. Yao, and B. Deng, “Fast and robust iterative closest point,” *IEEE Transactions on Pattern Analysis and Machine Intelligence*, vol. 44, no. 7, pp. 3450–3466, 2022.
- [15] L. Ma, H. Liang, B. Han, S. Yang, X. Zhang, and H. Liao, “Augmented reality navigation with ultrasound-assisted point cloud registration for percutaneous ablation of liver tumors,” *International journal of computer assisted radiology and surgery*, vol. 17, no. 9, pp. 1543–1552, 2022.
- [16] B. R. Thomson *et al.*, “Mr-to-us registration using multiclass segmentation of hepatic vasculature with a reduced 3d u-net,” in *International conference on medical image computing and computer-assisted intervention (MICCAI)*. Springer, 2020, pp. 275–284.
- [17] Q. Zeng *et al.*, “Learning-based us-mr liver image registration with spatial priors,” in *International conference on medical image computing and computer-assisted intervention (MICCAI)*. Springer, 2022, pp. 174–184.
- [18] S. Huang *et al.*, “One registration is worth two segmentations,” in *International Conference on Medical Image Computing and Computer-Assisted Intervention (MICCAI)*. Springer, 2024, pp. 665–675.
- [19] A. Zaganidis, L. Sun, T. Duckett, and G. Cielniak, “Integrating deep semantic segmentation into 3-d point cloud registration,” *IEEE Robotics and automation letters*, vol. 3, no. 4, pp. 2942–2949, 2018.
- [20] Q. Wang, Y. Yang, T. Wan, and S. Du, “Robust point set registration based on semantic information,” in *2020 IEEE International Conference on Systems, Man, and Cybernetics (SMC)*. IEEE, 2020.
- [21] J. Wasserthal *et al.*, “Totalsegmentator: robust segmentation of 104 anatomic structures in ct images,” *Radiology: Artificial Intelligence*, vol. 5, no. 5, p. e230024, 2023.
- [22] K. Stephens, “Clarius launches t-mode ai for ultrasound,” *AXIS Imaging News*, 2024.
- [23] M. Hiep *et al.*, “Real-time intraoperative ultrasound registration for accurate surgical navigation in patients with pelvic malignancies,” *International journal of computer assisted radiology and surgery*, vol. 20, no. 2, pp. 249–258, 2025.
- [24] Z. Jiang, Y. Kang, Y. Bi, X. Li, C. Li, and N. Navab, “Class-aware cartilage segmentation for autonomous us-ct registration in robotic intercostal ultrasound imaging,” *IEEE Transactions on Automation Science and Engineering*, vol. 22, pp. 4818 – 4830, 2025.
- [25] S. Khallaghi *et al.*, “Biomechanically constrained surface registration: Application to mr-trus fusion for prostate interventions,” *IEEE transactions on medical imaging*, vol. 34, no. 11, pp. 2404–2414, 2015.
- [26] M. Ringel, J. Heiselman, W. Richey, I. Meszoely, and M. Miga, “Regularized kelvinlet functions to model linear elasticity for image-to-physical registration of the breast,” in *International Conference on Medical Image Computing and Computer-Assisted Intervention (MICCAI)*. Springer, 2023, pp. 344–353.
- [27] Z. Yang, R. Simon, K. Merrell, and C. A. Linte, “Boundary constraint-free biomechanical model-based surface matching for intraoperative liver deformation correction,” *IEEE Transactions on Medical Imaging*, vol. 44, no. 4, pp. 1723–1734, 2025.
- [28] Y. Fu *et al.*, “Biomechanically constrained non-rigid mr-trus prostate registration using deep learning based 3d point cloud matching,” *Medical image analysis*, vol. 67, p. 101845, 2021.
- [29] —, “Deformable mr-cbct prostate registration using biomechanically constrained deep learning networks,” *Medical physics*, vol. 48, no. 1, pp. 253–263, 2021.
- [30] D. Wang, S. Azadvar, J. Heiselman, X. Jiang, M. Miga, and L. Wang, “Libr+: Improving intraoperative liver registration by learning the residual of biomechanics-based deformable registration,” in *International Conference on Medical Image Computing and Computer-Assisted Intervention (MICCAI)*. Springer, 2024, pp. 359–368.
- [31] C. Broit, *Optimal registration of deformed images*. University of Pennsylvania, 1981.
- [32] B. Fischer and J. Modersitzki, “Ill-posed medicine—an introduction to image registration,” *Inverse problems*, vol. 24, no. 3, p. 034008, 2008.
- [33] G. Nir *et al.*, “Model-based registration of ex vivo and in vivo mri of the prostate using elastography,” *IEEE transactions on medical imaging*, vol. 32, no. 6, pp. 1068–1080, 2013.
- [34] M. P. Heinrich, A. Bigalke, C. Großbröhmer, and L. Hansen, “Chasing clouds: differentiable volumetric rasterisation of point clouds as a highly efficient and accurate loss for large-scale deformable 3d registration,” in *Proceedings of the IEEE/CVF international conference on computer vision (ICCV)*, 2023, pp. 8026–8036.
- [35] M. P. Heinrich, A. Bigalke, and L. Hansen, “Fast forward: Rephrasing 3d deformable image registration through density alignment and splatting,” in *Medical Imaging with Deep Learning*, 2025.
- [36] F. Bernardini, J. Mittleman, H. Rushmeier, C. Silva, and G. Taubin, “The ball-pivoting algorithm for surface reconstruction,” *IEEE transactions on visualization and computer graphics*, vol. 5, no. 4, pp. 349–359, 2002.
- [37] D. Kingma and J. Ba, “Adam: A method for stochastic optimization,” *arXiv preprint arXiv:1412.6980*, 2014.
- [38] A. Segal, D. Haehnel, and S. Thrun, “Generalized-icp,” in *Robotics: science and systems*, vol. 2, no. 4. Seattle, WA, 2009, p. 435.
- [39] B. Fischer and J. Modersitzki, “A unified approach to fast image registration and a new curvature based registration technique,” *Linear Algebra and its applications*, vol. 380, pp. 107–124, 2004.
- [40] A. Hering *et al.*, “Learn2reg: comprehensive multi-task medical image registration challenge, dataset and evaluation in the era of deep learning,” *IEEE Transactions on Medical Imaging*, vol. 42, no. 3, pp. 697–712, 2022.
- [41] A. Fedorov *et al.*, “3d slicer as an image computing platform for the quantitative imaging network,” *Magnetic resonance imaging*, vol. 30, no. 9, pp. 1323–1341, 2012.
- [42] A. Lasso, T. Heffter, A. Rankin, C. Pinter, T. Ungi, and G. Fichtinger, “Plus: open-source toolkit for ultrasound-guided intervention systems,” *IEEE transactions on biomedical engineering*, vol. 61, no. 10, pp. 2527–2537, 2014.
- [43] K. Clark *et al.*, “The cancer imaging archive (tcia): maintaining and operating a public information repository,” *Journal of digital imaging*, vol. 26, pp. 1045–1057, 2013.
- [44] A. L. Simpson *et al.*, “A large annotated medical image dataset for the development and evaluation of segmentation algorithms,” *arXiv preprint arXiv:1902.09063*, 2019.
- [45] E. Chen, J. Novakofski, W. Jenkins, and W. O’Brien, “Young’s modulus measurements of soft tissues with application to elasticity imaging,” *IEEE Transactions on Ultrasonics, Ferroelectrics, and Frequency Control*, vol. 43, no. 1, pp. 191–194, 1996.
- [46] K. Brock, M. Sharpe, L. Dawson, S. Kim, and D. Jaffray, “Accuracy of finite element model-based multi-organ deformable image registration,” *Medical physics*, vol. 32, no. 6Part1, pp. 1647–1659, 2005.
- [47] S. Kruse *et al.*, “Tissue characterization using magnetic resonance elastography: preliminary results,” *Physics in Medicine & Biology*, vol. 45, no. 6, p. 1579, 2000.
- [48] M. C. Murphy, J. Huston III, and R. L. Ehman, “Mr elastography of the brain and its application in neurological diseases,” *Neuroimage*, vol. 187, pp. 176–183, 2019.
- [49] Y. Chi, J. Liang, and D. Yan, “A material sensitivity study on the accuracy of deformable organ registration using linear biomechanical models a,” *Medical physics*, vol. 33, no. 2, pp. 421–433, 2006.
- [50] A. Al-Mayah, J. Moseley, M. Velec, and K. Brock, “Toward efficient biomechanical-based deformable image registration of lungs for image-guided radiotherapy,” *Physics in Medicine & Biology*, vol. 56, no. 15, p. 4701, 2011.